Full Length Article

Spherical cluster method for ground state determination of site-disordered materials: Application to $Ag_xBi_yI_{x+3y}$

Victor T. Barone [a],[*], Blair R. Tuttle [b], Sanjay V. Khare [a]

[a] *Department of Physics, Wright Center for Photovoltaics Innovation and Commercialization, University of Toledo, Toledo, OH 43606, USA*
[b] *Department of Physics, Penn State Behrend, Erie, PA 16563, USA*

ARTICLE INFO

ABSTRACT

Silver bismuth-iodides ($Ag_xBi_yI_{x+3y}$) are a promising class of materials with potential for use as absorber layers in optoelectronic devices, but theoretical investigations into their properties are hindered by their large degree of site-disorder and unique layered structures. Here, we demonstrate a cluster-based description of the total energy that, paired with a simulated annealing minimizer, can create low-energy atomic models of $Ag_xBi_yI_{x+3y}$ from a pool of over 10^{100} possible choices. We employ *first principles* density functional theory to calculate band gaps, densities of states, effective masses, and absorption spectra of the ground state structures. Lattice constants, band gaps, and optical spectra of the structures compare favorably with available experimental results. This work additionally provides new insights into the physical and electronic structure of the more complicated Ag-Bi-I stoichiometries. The models generated can be used to gain insight on the role of various defects on the growth and properties of these materials.

1. Introduction

Silver bismuth-iodides (compounds with a generic formula $Ag_xBi_yI_{x+3y}$) are being developed for use in optoelectronics because of their efficient absorption across the optical and UV spectra [1–5]. Importantly, these materials can be easily grown over flexible substrates [6–10] and are more environmentally friendly than lead-based perovskites [10,11].

Ag-Bi-I systems often crystalize with stoichiometries $AgBiI_4$, $AgBi_2I_5$, Ag_3BiI_6, and $AgBi_2I_7$, having either cubic or trigonal symmetry [12–16]. Turkevych *et al.* [12] noted that the trigonal structures followed the $NaVO_2$ structure but with site-disordered layers of Ag, Bi, and vacancies (Va). Occupancy fractions are layer dependent. Despite this general understanding, construction of atomic models with no sites partially occupied has been an outstanding challenge. Atomic model construction of the four aforementioned stoichiometries necessitates the use of cells that have between 24 ($AgBiI_4$) and 294 ($AgBi_2I_7$) Ag/Bi/Va sites at minimum due to charge neutrality and stoichiometry restrictions. Choosing the explicit arrangements of silver, bismuth and vacancies to occupy these sites is a combinatorically difficult problem, e.g. the 294 atom case of $AgBi_2I_7$ has over 10^{100} possible solutions.

Several methods and programmatic implementations have been used to examine site-disordered materials [17–29]. Many are not suited to the current problem – the virtual crystal approximation is inapplicable to substitutional systems with significantly differing electronic configurations [20] and the special quasi-random structure (SQS) [26] technique predicts $AgBiI_4$ to be metallic [30,31], in contrast to experiment. The SQS likely fails for silver bismuth-iodides because only low-energy models yield electronic properties that compare well to experimental data. The simplest example of this is **Fig. S1**, where we show the relationship between band gaps of 9200 $AgBiI_4$ models and their energies.

To search for the ground state atomic arrangements for silver bismuth-iodides, we attempted machine-learning based approaches (sometimes called 'chemical fingerprints') [35–39], which failed to capture the physics of these materials when vacancies were introduced. Further, implementations of these and similar techniques, such as the cluster expansion [17,19,23–25,29], are unable to easily handle the layer-dependent partial occupancy rules. We therefore employ a spherical cluster model description of the energy paired with a simulated annealing minimization approach to successfully find ground states for four layered Ag-Bi-I stoichiometries out of (up to) $\sim 10^{100}$ possible solutions. We compute the properties of these models and find band gaps, optical absorption spectra, and lattice constants in agreement with experiment.

---

* Corresponding author.
E-mail address: vbarone@rockets.utoledo.edu (V.T. Barone).

2. Models & methods

2.1. Models

As described in Turkevych *et al.* [12], trigonal Ag-Bi-I materials are described by stacked layers whose site occupancies satisfy a set of linear equations. Our atomic models are repeats of the unit cell shown in Fig. 1. We consider the smallest models that (1) allow the solution of the system of equations to represent integer site occupancies and (2) allow the a and b axes to be equal in length, listed in Table 1.

Every entry in Table 1 represents many possible cell configurations. The **Supplementary information** details the method for calculating the total number of cell configurations. For each entry, the method described in **Section 2.2** and **Section 2.3** is used to predict the ten lowest energy structures. We then perform accurate DFT calculations on each to determine the ground state structure. The first row of Table 1 indicates the lowest energy structure found. Table 1 also indicates, with the exception of $AgBi_2I_7$, the number of unit cell repeats contained in the models discussed in **Section 3**. $AgBi_2I_7$'s $7 \times 7 \times 1$ model is too large for accurate optoelectronic DFT calculations, so we instead use a $4 \times 4 \times 1$ cell with stoichiometry $Ag_{1.0}Bi_{1.9}I_{6.9}$. This reduced the maximum number of combinations in the remaining models to 10^{60}.

2.2. Simulated annealing

Simulated annealing is a technique well-suited for optimizing discrete functions with multiple minima [32–34]. The goal of simulated annealing is to find the global optimum of a function by slowly reducing the ability of a candidate solution to get stuck in a higher energy state. To begin, we set an initial state as a configuration of atoms S_0 with energy $E(S_0)$, a starting thermal energy τ_0 (defined below), and a number of steps N. For each step j from 1 to N, a 'neighbor' state S_j of the last configuration S_{j-1} is generated (here, S_j is created by swapping a

FIG. 1. The $NaVO_2$-type unit cell of the Ag-Bi-I materials considered in this work. Each cell contains six iodine sites (black dots) and six sites whose occupancies vary between Ag, Bi, and Va (red/blue/white dots). The partially occupied sites are split into interchanging layers along the c direction with occupancy fractions per layer given in Table 1. (For interpretation of the references to colour in this figure legend, the reader is referred to the web version of this article.)

pair of atoms from S_{j-1}). S_j may or may not be accepted to replace S_{j-1} with probability P given by

$$P = \begin{cases} \exp\left[-\left(E(S_j) - E(S_{j-1})\right)/\tau_j\right] & \text{if } E(S_{j-1}) < E(S_j) \\ 1 & \text{otherwise} \end{cases}.$$

The sole parameter controlling the convergence to an optimal solution is the thermal energy τ. Large values of τ cause the algorithm to resemble a random search (since most swaps are accepted) and the system stays in a high energy state. Small values of τ cause the algorithm to emulate a steepest-descent minimization and only the closest local minimum is found. If the decrease in τ is gradual enough, the algorithm settles to the global minimum. We calculate τ with a geometrical cooling-schedule [35]:

$$\tau_j = \left[\tau_0\left(1 - \frac{j}{N}\right)^4\right]\left[\frac{E(S_{opt})}{E(S_{j-1})}\right]$$

where $E(S_{opt})$ is the lowest energy found up to j. The second term in brackets increases τ_j at non-optimal solutions, improving convergence near the end of the routine [36].

In this study, we fixed $\tau_0 = 5$ meV/site and $N = 2.2 \times 10^9$. N was chosen based on Fig. 2, where we show that for a large $7 \times 7 \times 1$ $AgBi_2I_7$ cell with no layering restrictions (10^{119} combinations), the minimum energy structure is identified in less than 10^{10} steps. Since the present models have orders of magnitude fewer combinations, we are confident that the global minimum structure is identified within 2.2×10^9 steps. In Fig. 3, the convergence of the same cell's predicted energy is plotted vs. the annealing progress. The minimum energy found during the first portion of the algorithm is over 100 meV/atom higher than the predicted ground state energy, indicating that a simple random search would be unlikely to identify low-energy structures.

2.3. Spherical cluster method

To predict the energy of a set of atoms, each site in a crystal system is described by its local 'cluster' σ, defined as a central site and all other sites within a cutoff radius of the central site. In contrast, the standard cluster expansion method [17,37–40], defines clusters based on the number of sites. Each spherical cluster has an energy associated with it; thus, each lattice site's energy is found through its defining cluster. Cluster energies are fit to DFT calculations through a linear model. The total energy of the crystal is then calculated as the sum of all lattice site energies. Importantly, in addition to Ag, Bi and I, vacant lattice sites also have an energy associated with them. Any given lattice site may be involved in multiple clusters.

The present method is advantageous in that energy predictions with spherical clusters converge faster than with arbitrarily shaped clusters such as singlets, doublets, etc. [28]). The improved convergence can be explained by considering each lattice site's energy as an 'embedding energy' similar to those used in force field models [41–43] (note, however, that the SCM is unable to calculate atomic forces). An atom's embedding energy is most strongly dependent on its first nearest neighbors, so a spherical cluster including all n first nearest neighbors will be a better description of its embedding energy than any other cluster of n sites.

The number of fitting parameters, and thus the number of DFT calculations needed to complete the fit, is greatly reduced by identifying clusters that are physically equivalent. Two clusters σ_j and σ_k are considered the same if: (1) the species counts between σ_j and σ_k are identical and (2) the 4D distances between all sites in σ_j are identical to those in σ_k. The 4D distance is calculated through the three cartesian dimensions and an index unique to each species. Under these rules, all clusters are invariant under translations, rotations, and inversions, which is physically sound (a cluster should not change its energy if it is rotated, for example).
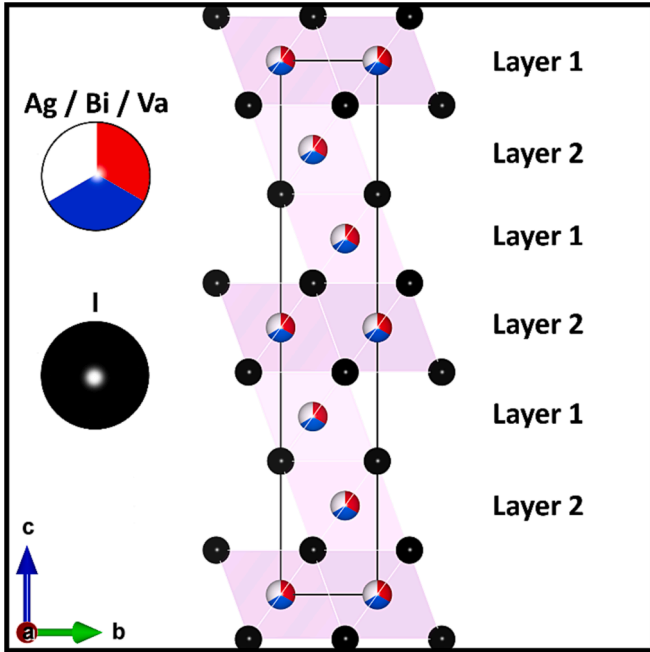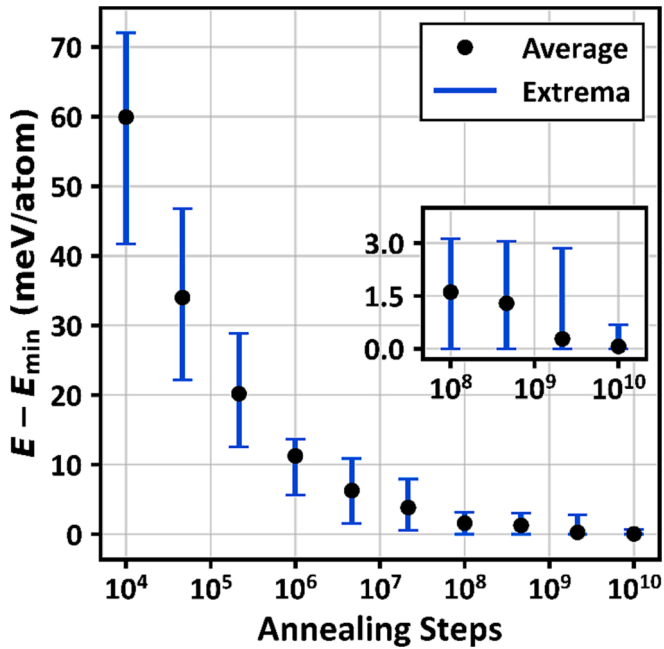
Table 1

Fractional occupancies for different layers of trigonal Ag-Bi-I cells that satisfy the system of equations given in Turkevych et al. [12]. The notation '(0, 1, 3): (2,1,1)/4', or example, means that any given site in layer 1 is occupied by 0% Ag, 25% Bi, and 75% Va, and any given site in layer 2 is occupied by 50% Ag, 25% Bi, and 25% Va. Also listed are the smallest cell sizes that satisfy $a = b$ and allow for integer site occupancies. Row 1 are the layer rules resulting in the lowest energy structures.

$AgBiI_4(2 \times 2 \times 1)$	$Ag_2BiI_5(5 \times 5 \times 1)$	$Ag_3BiI_6(3 \times 3 \times 1)$	$AgBi_2I_7(7 \times 7 \times 1)$
Layer 1:Layer 2	**Layer 1:Layer 2**	**Layer 1:Layer 2**	**Layer 1:Layer 2**
(1,1,2):(1,1,2)/4	(2,0,3):(2,2,1)/5	(1,0,2):(2,1,0)/3[a]	(0,2,5):(2,2,3)/7
(0,1,3):(2,1,1)/4[a]	(0,1,4):(4,1,0)/5	(0, 1, 2):(3,0,0)/3	(1,2,4):(1,2,4)/7
(0,2,2):(2,0,2)/4	(1,2,2):(3,0,2)/5	(1,1,1):(2,0,1)/3	(0,3,4):(2,1,4)/7
(1,0,3):(1,2,1)/4	(1,0,4):(3,2,0)/5[a]	–	(0,1,6):(2,3,2)/7
–	(2,1,2):(2,1,2)/5	–	(1,0,6):(1,4,2)/7[a]
–	(1,1,3):(3,1,1)/5	–	(1,1,5):(1,3,3)/7
–	(0,2,3):(4,0,1)/5	–	(0,4,3):(2,0,5)/7

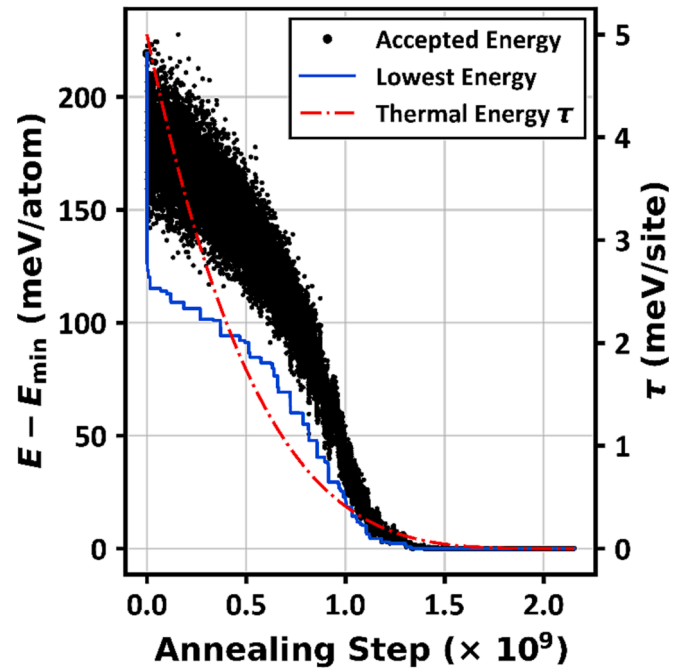[a] Occupancy rule given in Turkevych et al. [12].

FIG. 2. Simulated annealing solutions vs. the number of annealing steps for a $7 \times 7 \times 1$ cell (294 exchangeable sites) of $AgBi_2I_7$. Table 1's rules were not applied, maximizing the complexity. Black dots and blue bars represent the average and extrema of 10 independent runs. **(inset)** The minimum extrema energies of the last four data sets are all equal, indicating convergence. (For interpretation of the references to colour in this figure legend, the reader is referred to the web version of this article.)

FIG. 3. Evolution of the accepted SCM energy and thermal energy τ during simulated annealing of $AgBi_2I_7$. Accepted energies (black dots) are recorded every 2^{16} steps, while the optimal energy (blue line) is updated at every step, which is why the lowest energy appears lower than the accepted energies for steps below 10^9. The multiplicative noise parameter is removed from τ for clarity. (For interpretation of the references to colour in this figure legend, the reader is referred to the web version of this article.)

Even with the above considerations, materials with many species or neighbors may result in an unwieldy number of clusters to fit. Shapeev [28,44] previously used a low-rank tensor approximation to solve a similar issue for high entropy alloys. An analogous method to the present SCM would be to approximate the fitting matrix with its low-rank representation found through, say, the singular value decomposition [45].

Using a search radius cutoff of 3.1 Å (1st nearest-neighbors) resulted in 92 7-site clusters for Ag-Bi-I compounds. We use 5 training cells per cluster for proper sampling, resulting in a total of 460 DFT calculations for fitting the model. The aforementioned low rank approximation is unnecessary for the current situation.

2.4. Density functional theory calculations

We use the Vienna *ab initio* Simulation Package (VASP version 6.1.0 [46–48]) for all DFT [49,50] calculations. We treat exchange–correlation effects with the semi-local Perdew–Burke–Ernzerhof (PBE) functional [51]. Standard PAW potentials are used to represent the core electrons [52,53]; ($4d^{10} 5 s^1$), ($6 s^2 6p^3$) and ($5 s^2 5p^5$) valence electrons were included for silver, bismuth, and iodine, respectively. We have tested approximations other than GGA-PBE, but found no clear reason to use them. A summary of these tests is given in the **supplemental information**.

For SCM fitting / testing, the Γ point is used for Brillouin Zone integrations and the plane wave basis is cut off at 250 eV. All other calculations employ plane waves with energy up to 330 eV and regular k-point meshes with spacings of approximately 40 and 60 $(1/\text{Å})^{-1}$ for geometry and optoelectronic calculations, respectively.

We fix the iodine sites at their crystallographic positions during the structural relaxations. Molecular dynamics simulations indicate that the iodine crystallographic positions are dynamically stable at room temperature (see **Fig. S2**), which also agrees with experimental XRD results (see **Fig. S3**).

For Ag-Bi-I materials, previous work [14,54–56] has shown that band gap values computed within the generalized gradient approximation (GGA) are comparable to those calculated with the more expensive approach including the HSE06 (Heyd-Scuseria-Ernzerhof [57]) functional and spin–orbit coupling (SOC) also accounted for. We confirm this to be true for a few AgBiI$_4$ structures, see Section 3.4. The overall structure and compositions of all Ag-Bi-I materials studied here are similar to AgBiI$_4$, so we expect the present GGA optoelectronic calculations to be accurate.

Effective masses are calculated as described by Hauiter *et al.* [58], as an average over the thermally active band-edge states:

$$\langle M_{ij}^{-1} \rangle = -\frac{\sum_{b=bands} \int \frac{d^3\mathbf{k}}{(2\pi)^3} \frac{1}{\hbar^2} \frac{\partial^2 E_b(\mathbf{k})}{\partial k_i \partial k_j} n_{FD}(\mathbf{k})}{\sum_{b=bands} \int \frac{d^3\mathbf{k}}{(2\pi)^3} n_{FD}(\mathbf{k})}$$

where $E_b(\mathbf{k})$ is the energy of band b at point $\mathbf{k}$ and $n_{FD} = (\exp[\pm(E_b(\mathbf{k}) - \mu)/(kT)] + 1)^{-1}$ is the Fermi-Dirac distribution at chemical potential μ (chosen to be just below/above the band edges) and temperature T (treated as a variable). This results in an effective mass tensor, $\langle M_{ij} \rangle$, whose eigenvalues are averaged to yield the effective masses reported here. The dielectric response functions are calculated through VASP's implementation of the formalism described by Gajdoš *et al.* [59], and corrected with the method of Nishiwaki and Fujiwara [60].

3. Results

3.1. Spherical cluster method

In Fig. 4, we show the quality of the SCM (Fig. 4.e) compared to some other chemical fingerprint methods (Fig. 4.a-d). Similar to our reasoning for training on 460 simulation cells (92 total environments, 5 cells per environment), our verification set is 9200 unique representations of AgBiI$_4$ (92 environments, 100 cells per environment) to ensure that each chemical environment is tested. Other than the guarantee that each testing cell has at least one specific environment, they are completely randomized. For Fig. 4.a-d, an 80–20 train-test split is applied to these structures, as is common practice in the machine learning community. The SCM in Fig. 4.e is fit with a 5–95 split. We apply linear regression (LR), kernel ridge regression (KRR), and decision tree regression (DTR), to a descriptor used in our previous work on cubic AgBiI$_4$ [54] (nearest-neighbor metal pair counts, NNMPC, Fig. 4.a) as well as three other common descriptors: orbital field matrix (OFM) [61], coulomb matrix (CM, Fig. 4.c) [62], and a cell-periodic extension to CM (CM+, Fig. 4.d) [63]. Fig. 4.b, shows a variant of the OFM that treats local contributions individually since the original version does not distinguish between site-disordered structures. We only show the best performing methods in Fig. 4.a-d - see Fig. S4 and S5 for all methods applied to trigonal and cubic AgBiI$_4$.

For trigonal AgBiI$_4$ (Fig. 4, black dots), the SCM is the only descriptor tested capable of a mean absolute error (mae) <15 meV/atom. The mae values of Fig. 4.a-d range from 30 to 55 meV/atom for the trigonal structures. The SCM's mae is 11 meV/atom, achieved with 6% of the training data of the other descriptors. For cubic AgBiI$_4$ (Fig. 4, red crosses), all methods perform much better (maes of 5–2 and 2 meV/atom for Fig. 4.a-d and the SCM, respectively). Where other fingerprints show great improvement in relative fitting error from trigonal to cubic AgBiI$_4$, the SCM's error is 2–3% of the total energy span in both cases.

The speed of the SCM's energy evaluations is another benefit, especially in difficult optimization problems such as the 294-site problem shown in Fig. 2 and Fig. 3. The fact that the OFM, CM, and CM+ fingerprints require the solutions to eigenvalue problems means that they scale much worse than the SCM as the system size grows: with n the total number of sites and m the number of sites per cluster, the time
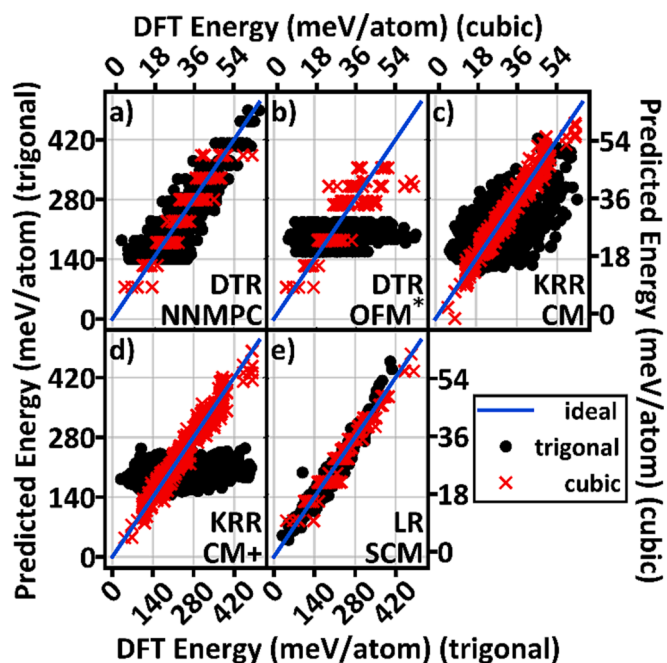

FIG. 4. Performance of energy descriptors for AgBiI$_4$. In a-d), an 80–20 train-test split is applied to 9200 and 12870 AgBiI$_4$ models for the trigonal and cubic cases, respectively. In e), a 5–95 and 0.2–99.8 train-test split is applied to the corresponding models for trigonal and cubic symmetry, respectively. Training points are not shown. The blue line is an ideal fit. Each subplot represents the best (lowest mean absolute error) performance of a chemical descriptor given three fitting methods: linear regression (LR), kernel ridge regression (KRR), and decision tree regression (DTR). The chemical descriptors are: a) nearest-neighbor metal pair counts (NNMPC) [54], b) Orbital Field Matrix* (OFM) [61], c) Coulomb Matrix (CM) [62], d) Extended Coulomb Matrix (CM+) [63], e) spherical cluster method (SCM). *: We use an altered version of the OFM. See Section 3.1. (For interpretation of the references to colour in this figure legend, the reader is referred to the web version of this article.)

complexity of our SCM is $\mathcal{O}(nm^2)$, while eigenvalue algorithms have $\mathcal{O}(n^3)$ complexity [45]. Treating consecutive simulated annealing steps as perturbations reduces the SCM's complexity to $\mathcal{O}(m^2)$, but the authors are unaware of any analogous methods for eigenvalues.

3.2. Comparison with cubic AgBiI$_4$

We now discuss the differences in fit quality between trigonal and cubic AgBiI$_4$. Cubic AgBiI$_4$'s general structure has been described in references [13,14,56]. The models employed here are identical to those used in our previous work [54]. Both structures are comprised of tetrahedra featuring central Ag/Bi/Va sites surrounded by six iodine atoms. Positions of Va in cubic AgBiI$_4$ can be determined through XRD patterns [56], so our models only involved site disorder with Ag and Bi. An example model is shown in Fig. S6.

For testing descriptors on the cubic models, we train new predictive models for the NNMPC, OFM, CM, CM+, and SCM exclusively on cubic cells. SCM analysis of the cubic models reveals that there are only 6 unique chemical environments. To stay consistent with the method applied to the trigonal structures, we fit the SCM with 30 = (6 unique environments) × (5 cells per environment) training points. The other chemical descriptors are trained on 80% of the 12870 cubic structures, as was done in Section 3.1.

All of the descriptors shown in Fig. 4. provide acceptable fits to cubic AgBiI$_4$'s energies. When the same descriptors are applied to trigonal AgBiI$_4$, however, only the SCM gives results accurate enough for quantitative determination of the ground state structures. We propose the

following rationale behind this discrepancy: The CM, CM+, and OFM fingerprints are "global" descriptors in the sense that they build matrices as functions of atomic positions and types over the entire cell. The descriptor is then vectorized as the eigenvalues of those matrices. The inclusion of vacancies causes too large a range of possible energies for such a treatment - compare the 57 meV/atom energy range for cubic $AgBiI_4$ to the 477 meV/atom range for trigonal $AgBiI_4$. Attempting to describe such an energy range with global descriptors is a difficult task even for nonlinear fitting techniques such as KRR or DTR. The NNMPC, although not a "global" descriptor, cannot account for the high variance of local environments that depend on more than just pairwise interactions.

The SCM bypasses the aforementioned issues because it is a strictly local descriptor that accounts for each possible environment individually – every site is explicitly described as a function of its neighbors and the contributions are added. This method is well-suited for describing the total energy since it is an additive quantity. Any deviations in the bond ordering of an atom are contained in a unique cluster instead of being lost in the global description. By this logic, we would expect the SCM to be most appropriate for any site-disordered material with a wide range of local interaction energies including the present silver bismuth-iodides, their alloys [10,55,64], $CuBiI_4$ [5] and similar systems.

We examined the individual cluster energies vs. the vacancy concentration, shown in **Fig. S7**. One may expect the spread of energies to grow as the number of vacancies in each cluster grew, but this is not the case for our fit. This is likely because the number of Ag and Bi atoms are not held constant – these two atoms have significantly different electronic structures, and thus have a wide range of interaction energies, especially when also "coordinated" by vacancies. Such an effect was noted in Shapeev's work [28] as well, where the RMSE of his cluster expansions grew with the number of elements from different groups.

3.3. Structural, mechanical properties

For ground state structures, we calculated lattice constants through the minima of energy-strain curves, obtaining $(a, c) = (4.46, 21.36)$, $(4.45, 21.28)$, $(4.43, 21.21)$, and $(4.46, 21.36)$ Å for $AgBiI_4$, $AgBi_2I_5$, Ag_3BiI_6, and $AgBi_2I_7$, respectively. These values are about 3% larger than experimental results for $AgBiI_4$, $AgBi_2I_5$, Ag_3BiI_6, and $AgBi_2I_7$ [8,13,16,56,64], as expected for DFT using the PBE functional. The identical results between $AgBiI_4$ and $AgBi_2I_7$ may be explained by Xiao *et al.*'s [14] recent report that the structure of $AgBi_2I_7$ is very similar to $AgBiI_4$ with a slight silver deficiency.

Through the energy-strain curves used for the lattice constant determination, we also calculate the bulk moduli. For Ag_3BiI_6, the bulk modulus is 24 GPa whereas for the other three stoichiometries the bulk moduli are 25 GPa. Interestingly, the variance in vacancy concentration (between 20% and 30% of all sites depending on stoichiometry) does not seem to have a major effect on the mechanical properties of Ag-Bi-I materials.

3.4. Band gaps, density of states

The indirect band gaps of the Ag-Bi-I structures found here are 1.8 eV for Ag_3BiI_6 and 1.7 eV for $AgBiI_4$, $AgBi_2I_5$, and $AgBi_2I_7$, all of which fall within the experimental indirect band gap range (1.7–1.9 eV) [6–9,11,15]. References [12,56] also measured direct gaps ranging from 1.6 to 1.8 eV.

Previous studies on Ag-Bi-I materials [14,54–56], as well as this work, have shown that band gaps calculated with the GGA and without including spin–orbit coupling (SOC) provide band gap results similar to those found using hybrid functionals with the inclusion of SOC. This has been attributed to a cancelation of errors involved in ignoring many-body effects (underestimating the band gap) and ignoring relativistic effects (overestimating the band gap) [65]. The inclusion of SOC is most important for materials involving heavy elements such as lead, or in the

present case, bismuth. For verification, we applied the HSE06 functional and included SOC on the two lowest energy cells of $AgBiI_4$. The differences in band gaps were less than 0.1 eV from the PBE result with no systematic trend. In cubic $AgBiI_4$, for the three lowest energy cells, we found that the gap difference was $\pm$ 0.1 eV on average. We conclude that our GGA band gaps agree with HSE06 + SOC gaps to within 0.1 eV, and thus the average band gaps of our Ag-Bi-I cells are 1.7 ± 0.1 eV, again within the range of existing experimental results.

The difference in direct and indirect gaps for each stoichiometry varies significantly. The greatest difference is for our $AgBi_2I_7$ model, which has a 250 meV difference between its direct and indirect band gaps. $AgBi_2I_7$'s experimental differences range from 110 to 210 meV [8,9,55]. For our $AgBiI_4$ model, we find a 120 meV difference in gap types while the experimental difference ranges from 80 to 750 meV [7,8,56]. The differences between direct / indirect gaps in our models of Ag_3BiI_6 and $AgBi_2I_5$ are less than 20 meV (below our numerical uncertainty). Experimental work indicates gap differences higher at 60 meV for Ag_3BiI_6 [6], and between 80 and 500 meV [7,8] for Ag_2BiI_5. While the variation of experimental results for each stoichiometry prevents a quantitative comparison between theory and experiment, our results do follow the experimental trend that the direct / indirect gap differences in $AgBiI_4$ / $AgBi_2I_7$ are generally larger than those in Ag_3BiI_6 / $AgBi_2I_5$.

The DOS in Fig. 5 reveals that the valence band edges for all stoichiometries are comprised mostly of silver and iodine states with little contribution from Bi. Most of silver's states are from the *d* orbitals, and most of iodine's states are from its *p* orbitals (individual angular momenta contributions are omitted from Fig. 5 for readability). Near the conduction band minimum, bismuth's and iodine's *p* orbitals make up most of the DOS. This is in agreement with previous work on $AgBiI_4$ [54,56]. Comparing the onset of the DOS near the Fermi level to the conduction band minimum also shows that the valence bands of all stoichiometries are relatively flat, especially compared to the conduction bands, in accordance with previous findings [14,54,56].

3.5. Effective masses

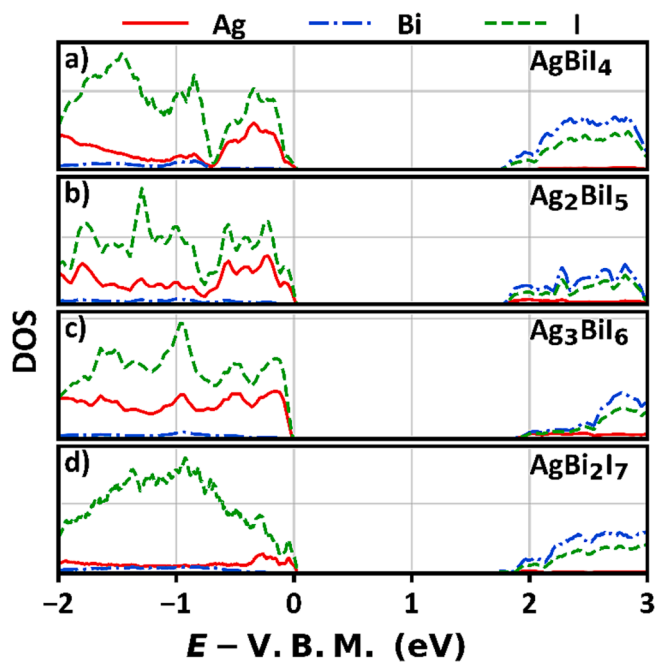Because of the large cells employed in the present study, there are

FIG. 5. Electronic PDOS for selected Ag-Bi-I structures from the first row of Table 1. **a)**, **b)**, **c)**, and **d)** represent $AgBiI_4$, $AgBi_2I_5$, Ag_3BiI_6, and $AgBi_2I_7$, respectively.

many bands near the band extrema, especially for the relatively flat valence bands of the present Ag-Bi-I materials. Thus, single band effective masses do not properly account for the actual effective mass in these materials. We instead calculate the effective mass tensor as an integrated average over all thermally active bands near the band edges [58]. Fig. 6 shows the 'conductivity masses', which are the harmonic mean of each tensor's eigen-masses. For simplicity, the chemical potentials involved in the thermal averages are fixed at 30 meV from the band edges.

For all stoichiometries considered, both electron and hole masses display a nearly linear increase with temperature. The rate of mass increase for electrons is modest at $\approx 0.004 m^*/m_0$ per K. The increase for holes is higher at about $\approx 0.02 m^*/m_0$ per K. As band states further from the band edges tend to have less curvature than those near the band edges, the increase in mass with temperature is mainly due to more far edge states being thermally activated. This effect is more pronounced for the valance bands, where the near band edge DOS is much higher than the DOS near the conduction band edges. At room temperature (300 K), the hole masses found range from $\approx 6.7 m_0$ (AgBi$_2$I$_5$) to $\approx 8.1 m_0$ (AgBi$_2$I$_7$) whereas the electron band masses range from $\approx 1.1 m_0$ (Ag$_3$BiI$_6$) to $\approx 1.6 m_0$ (AgBi$_2$I$_5$).

3.6. Absorption spectra

In Fig. 7, we report the calculated absorption coefficient between 0.5 and 5.0 eV for all four Ag-Bi-I stoichiometries considered. The PHS method [60] is applied to all components of the complex dielectric functions, shown in Fig. S8, using $\Delta E_g = \pm 0.1$ eV as our gap uncertainty input.

Compared to the experimental absorption coefficients, we find that our calculated absorption spectra tend to be larger in magnitude but show similar absorption onsets. The maxima of our absorption coefficients in the Visible / low UV range are between 6×10^5 and 7×10^5 cm^{-1} depending on stoichiometry. Sansom and Crovetto's groups [6,56] measured the absorption coefficients in Ag-Bi-I thin films to be between 2×10^5 and 5.5×10^5 cm^{-1}, though one of the films may have had an absorption coefficient as high as 10^6 cm^{-1}. Other experimental work
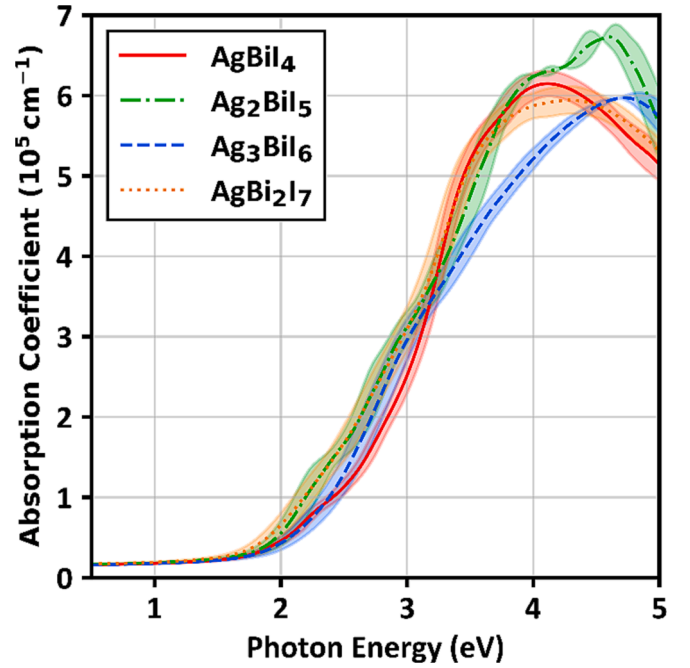
FIG. 7. PHS-corrected (PBE + HSE06 + Sum) [60] absorption spectra of Ag-Bi-I cells from the first row of Table 1. Filled regions represent deviations in the spectrum calculated with the PHS method for bandgap corrections of $\Delta E_g = \pm 0.1$ eV. The solid lines are averages over the filled regions.

[4,6–12,15,55,56,64] report absorption onsets at about 1.8 eV and relative absorption values, and we find that our results agree with both. While our calculations are for bulk models, the experiments are for thin films which may explain the higher peak values we find [66,67].

4. Conclusion

We construct and apply a new Spherical Cluster Method (SCM), which allows us to find ground state energy cells within the massive search space of Ag-Bi-I rudorffites. By comparing energy predictions of the SCM with some common chemical fingerprint methods, we determined that the SCM outperforms popular machine learning-based methods when describing the present Ag-Bi-I materials. The SCM method should also be efficient for examining other crystals with high degrees of site-disorder. It is especially well-suited for situations where the disordered sites may be occupied by species whose electronic structures are significantly different from one another (Ag / Bi / Va). Combining the SCM with a simulated annealing routine can effectively determine minimum energy cells for problems that have over 10^{100} possible configurations.

Focusing on one minimum-energy cell for each stoichiometry of Ag-Bi-I, we show that the method produces cells whose lattice constants (a = 4.4 – 4.5 Å, c = 21.2 – 21.4 Å), band gaps (1.7 – 1.8 eV), and absorption spectra agree well with experimental data. With the same cells, we also calculate the bulk moduli (24–25 GPa), electronic density of states, and conductivity effective masses. Effective mass calculations estimate that electrons are significantly lighter than holes in Ag-Bi-I materials, with electrons near room temperature having masses similar to free electrons, and holes being about seven times as massive. This knowledge is important when considering Ag-Bi-I materials for applications – devices should employ electrons, not holes, for conductivity.

The present results show a large improvement over current methods of finding low energy structures in site-disordered materials. Not only does the SCM seem to be more accurate, but it also scales better with system size than machine-learning-based approaches. This is especially
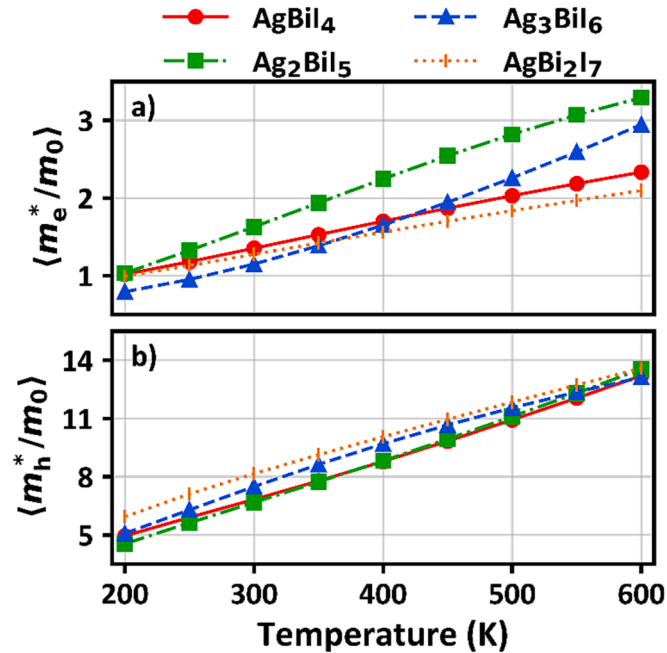
FIG. 6. Average conductivity effective masses of a) electrons and b) holes in selected minimum energy Ag-Bi-I cells from the first row of Table 1 at different temperatures. In each case, the chemical potential is fixed at 2% below (above) the conduction band minimum (valance band maximum) for electrons (holes).

important for materials that have to be described by large simulation cells.

In terms of photovoltaics, stoichiometries with lower concentrations of Bi should be the most performant [9,12,31]. By this measure, Ag_3BiI_6 and Ag_2BiI_5 would be the preferred stoichiometries for use in PV cells, yet the fact that $AgBiI_4$ and Ag_2BiI_7 can more easily be made to grow as single phases [12,13,16] has made them popular choices for use in proof-of-concept PV cells, despite their higher Bi concentrations. The method described here can produce accurate atomic models that could be employed to explore this efficiency-stability tradeoff – perhaps doping can be employed to increase PV performance or reduce phase segregation. Additionally, the models discovered could be used for large-scale cells appropriate for studying defects in these materials.

CRediT authorship contribution statement

Victor T. Barone: Conceptualization, Methodology, Software, Validation, Investigation. **Blair R. Tuttle:** Conceptualization, Validation, Supervision. **Sanjay V. Khare:** Conceptualization, Resources, Supervision, Project administration, Funding acquisition.

Declaration of Competing Interest

The authors declare that they have no known competing financial interests or personal relationships that could have appeared to influence the work reported in this paper.

Data availability

Data will be made available on request.

Acknowledgements

Appendix A. Supplementary material

See the supplementary material for the equation used for the calculation of the number of possible structures and data regarding how methods other than GGA-PBE affect structural and electronic properties. The band gap-energy relationship of the testing set (**Fig. S1**), statistics and simulated x-ray diffraction patterns from molecular dynamics simulations of $AgBiI_4$ (**Fig. S2** and **S3**), extra information relating to **Fig. 4** (**Fig. S4**, **S5**, and **S6**), a graph of fit 'cluster' energies (**Fig. S7**), and PHS-corrected dielectric functions used to produce **Fig. 7** (**Fig. S8**) are also included in the supplementary material.

Supplementary data to this article can be found online at https://doi.org/10.1016/j.commatsci.2023.112587.

References

[1] G. Kakavelakis, M. Gedda, A. Panagiotopoulos, E. Kymakis, T.D. Anthopoulos, K. Petridis, Metal Halide Perovskites for High-Energy Radiation Detection, Adv. Sci. 7 (2020) 2002098, https://doi.org/10.1002/advs.202002098.

[2] A.K. Jena, A. Kulkarni, T. Miyasaka, Halide Perovskite Photovoltaics: Background, Status, and Future Prospects, Chem. Rev. 119 (2019) 3036–3103, https://doi.org/10.1021/acs.chemrev.8b00539.

[3] D.H. Fabini, J.G. Labram, A.J. Lehner, J.S. Bechtel, H.A. Evans, A. Van der Ven, F. Wudl, M.L. Chabinyc, R. Seshadri, Main-Group Halide Semiconductors Derived from Perovskite: Distinguishing Chemical, Structural, and Electronic Aspects, Inorg. Chem. 56 (2017) 11–25, https://doi.org/10.1021/acs.inorgchem.6b01539.

[4] V. Pecunia, Y. Yuan, J. Zhao, K. Xia, Y. Wang, S. Duhm, L. Portilla, F. Li, Perovskite-Inspired Lead-Free Ag_2BiI_5 for Self-Powered NIR-Blind Visible Light Photodetection, Nano-Micro Lett. 12 (2020) 27, https://doi.org/10.1007/s40820-020-0371-0.

[5] A. Chakraborty, N. Pai, J. Zhao, B.R. Tuttle, A.N. Simonov, V. Pecunia, Rudorffites and Beyond: Perovskite-Inspired Silver/Copper Pnictohalides for Next-Generation Environmentally Friendly Photovoltaics and Optoelectronics, Adv. Funct. Mater. 32 (2022) 2203300, https://doi.org/10.1002/adfm.202203300.

[6] A. Crovetto, A. Hajijafarassar, O. Hansen, B. Seger, I. Chorkendorff, P.C.K. Vesborg, Parallel Evaluation of the BiI_3, $BiOI$, and Ag_3BiI_6 Layered Photoabsorbers, Chem. Mater. 32 (2020) 3385–3395, https://doi.org/10.1021/acs.chemmater.9b04925.

[7] B. Ghosh, B. Wu, X. Guo, P.C. Harikesh, R.A. John, T. Baikie, A.T.S. Arramel, C. Wee, T.C. Guet, S. Sum, N.M. Mhaisalkar, Superior Performance of Silver Bismuth Iodide Photovoltaics Fabricated via Dynamic Hot-Casting Method under Ambient Conditions, Adv. Energy Mater. 8 (2018) 1802051, https://doi.org/10.1002/aenm.201802051.

[8] M. Khazaee, K. Sardashti, C.-C. Chung, J.-P. Sun, H. Zhou, E. Bergmann, W. A. Dunlap-Shohl, Q. Han, I.G. Hill, J.L. Jones, D.C. Lupascu, D.B. Mitzi, Dual-source evaporation of silver bismuth iodide films for planar junction solar cells, J. Mater. Chem. A. 7 (2019) 2095–2105, https://doi.org/10.1039/C8TA08679F.

[9] Y. Kim, Z. Yang, A. Jain, O. Voznyy, G.-H. Kim, M. Liu, L.N. Quan, F.P. García de Arquer, R. Comin, J.Z. Fan, E.H. Sargent, Pure Cubic-Phase Hybrid Iodobismuthates $AgBi_2I_7$ for Thin-Film Photovoltaics, Angew. Chem. Int. Ed. 55 (2016) 9586–9590, https://doi.org/10.1002/anie.201603608.

[10] H. Wu, H. Zhu, A. Erbing, M.B. Johansson, S. Mukherjee, G.J. Man, H. Rensmo, M. Odelius, E.M.J. Johansson, Bandgap Tuning of Silver Bismuth Iodide via Controllable Bromide Substitution for Improved Photovoltaic Performance, ACS Appl. Energy Mater. 2 (2019) 5356–5362, https://doi.org/10.1021/acsaem.9b00914.

[11] C. Lu, J. Zhang, H. Sun, D. Hou, X. Gan, M. Shang, Y. Li, Z. Hu, Y. Zhu, L. Han, Inorganic and Lead-Free $AgBiI_4$ Rudorffite for Stable Solar Cell Applications, ACS Appl. Energy Mater. 1 (2018) 4485–4492, https://doi.org/10.1021/acsaem.8b01202.

[12] I. Turkevych, S. Kazaoui, E. Ito, T. Urano, K. Yamada, H. Tomiyasu, H. Yamagishi, M. Kondo, S. Aramaki, Photovoltaic Rudorffites: Lead-Free Silver Bismuth Halides Alternative to Hybrid Lead Halide Perovskites, ChemSusChem 10 (2017) 3754–3759, https://doi.org/10.1002/cssc.201700980.

[13] T. Oldag, T. Aussieker, H.-L. Keller, C. Preitschaft, A. Pfitzner, Solvothermale Synthese und Bestimmung der Kristallstrukturen von $AgBiI_4$ und Ag_3BiI_6, Z. anorg. allg. Chem. 631 (2005) 677–682, https://doi.org/10.1002/zaac.200400508.

[14] Z. Xiao, W. Meng, D.B. Mitzi, Y. Yan, Crystal Structure of $AgBi_2I_7$ Thin Films, J. Phys. Chem. Lett. 7 (2016) 3903–3907, https://doi.org/10.1021/acs.jpclett.6b01834.

[15] H. Zhu, M. Pan, M.B. Johansson, E.M.J. Johansson, High Photon-to-Current Conversion in Solar Cells Based on Light-Absorbing Silver Bismuth Iodide, ChemSusChem 10 (2017) 2592–2596, https://doi.org/10.1002/cssc.201700634.

[16] L.F. Mashadieva, Z.S. Aliev, A.V. Shevelkov, M.B. Babanly, Experimental investigation of the Ag–Bi–I ternary system and thermodynamic properties of the ternary phases, J. Alloys Compounds. 551 (2013) 512–520, https://doi.org/10.1016/j.jallcom.2012.11.033.

[17] A. van de Walle, M. Asta, G. Ceder, The alloy theoretic automated toolkit: A user guide, Calphad 26 (2002) 539–553, https://doi.org/10.1016/S0364-5916(02)80006-2.

[18] P. Sánchez-Palencia, S. Hamad, P. Palacios, R. Grau-Crespo, K.T. Butler, Spinel nitride solid solutions: charting properties in the configurational space with explainable machine learning, Digital Discovery. 1 (2022) 665–678, https://doi.org/10.1039/D2DD00038E.

[19] R. Grau-Crespo, S. Hamad, C.R.A. Catlow, N.H. de Leeuw, Symmetry-adapted configurational modelling of fractional site occupancy in solids, J. Phys.: Condens. Matter. 19 (2007) 256201, https://doi.org/10.1088/0953-8984/19/25/256201.

[20] L. Bellaiche, D. Vanderbilt, Virtual crystal approximation revisited: Application to dielectric and piezoelectric properties of perovskites, Phys. Rev. B. 61 (2000) 7877–7882, https://doi.org/10.1103/PhysRevB.61.7877.

[21] L. Nordheim, Zur Elektronentheorie der Metalle. I, Annalen der Physik 401 (1931) 607–640, https://doi.org/10.1002/andp.19314010507.

[22] F. Yonezawa, K. Morigaki, Coherent Potential Approximation, Basic Concepts and Applications, Progress Theor. Phys. (1973) 1–76.

[23] J.H. Chang, D. Kleiven, M. Melander, J. Akola, J.M. Garcia-Lastra, T. Vegge, CLEASE: a versatile and user-friendly implementation of cluster expansion method,

J. Phys.: Condens. Matter. 31 (2019), 325901, https://doi.org/10.1088/1361-648X/ab1bbc.

[24] T. Yamashita, S. Kanehira, N. Sato, H. Kino, K. Terayama, H. Sawahata, T. Sato, F. Utsuno, K. Tsuda, T. Miyake, T. Oguchi, CrySPY: a crystal structure prediction tool accelerated by machine learning, Sci. Technol. Adv. Mater. Methods 1 (2021) 87–97, https://doi.org/10.1080/27660400.2021.1943171.

[25] J.J. Maldonis, Z. Xu, Z. Song, M. Yu, T. Mayeshiba, D. Morgan, P.M. Voyles, StructOpt: A modular materials structure optimization suite incorporating experimental data and simulated energies, Computat. Mater. Sci. 160 (2019) 1–8, https://doi.org/10.1016/j.commatsci.2018.12.052.

[26] A. Zunger, S.-H. Wei, L.G. Ferreira, J.E. Bernard, Special quasirandom structures, Phys. Rev. Lett. 65 (1990) 353–356, https://doi.org/10.1103/PhysRevLett.65.353.

[27] P.M. Sharp, M.S. Dyer, G.R. Darling, J.B. Claridge, M.J. Rosseinsky, Chemically directed structure evolution for crystal structure prediction, Phys. Chem. Chem. Phys. 22 (2020) 18205–18218, https://doi.org/10.1039/D0CP02206C.

[28] A. Shapeev, Accurate representation of formation energies of crystalline alloys with many components, Comput. Mater. Sci 139 (2017) 26–30, https://doi.org/10.1016/j.commatsci.2017.07.010.

[29] D. Lerch, O. Wieckhorst, G.L.W. Hart, R.W. Forcade, S. Müller, UNCLE: a code for constructing cluster expansions for arbitrary lattices with minimal user-input, Modell. Simul. Mater. Sci. Eng. 17 (2009), 055003, https://doi.org/10.1088/0965-0393/17/5/055003.

[30] C. Bruni, L. Pedesseau, J. Even, M. Kepenekian, G. Volonakis, Rudorffites for solar-cell applications: Insights on their structures, electronic and optical properties from first-principles, (2021). https://doi.org/10.5281/zenodo.5799064.

[31] B. Cucco, L. Pedesseau, C. Katan, J. Even, M. Kepenekian, G. Volonakis, Silver-Bismuth Halide Double Salts for Lead-Free Photovoltaics: Insights from Symmetry-Based Modeling, Solar RRL. 6 (2022) 2200718, https://doi.org/10.1002/solr.202200718.

[32] A. Khachaturyan, S. Semenovsovskaya, B. Vainshtein, The thermodynamic approach to the structure analysis of crystals, Acta Cryst. A. 37 (1981) 742–754, https://doi.org/10.1107/S0567739481001630.

[33] S. Kirkpatrick, C. Gelatt, M. Vecchi, Optimization by Simulated Annealing, Science 220 (1983) 671–680.

[34] N. Metropolis, A.W. Rosenbluth, M.N. Rosenbluth, A.H. Teller, E. Teller, Equation of State Calculations by Fast Computing Machines, J. Chem. Phys. 21 (1953) 1087–1092, https://doi.org/10.1063/1.1699114.

[35] W. Mahdi, S.A. Medjahed, M. Ouali, Performance Analysis of Simulated Annealing Cooling Schedules in the Context of Dense Image Matching, CyS. 21 (2017), https://doi.org/10.13053/cys-21-3-2553.

[36] V. Cicirello, Optimizing the Modified Lam Annealing Schedule, EAI Endorsed Trans. Ind. Networks Intell. Syst. 7 (2021), 167653, https://doi.org/10.4108/eai.16-12-2020.167653.

[37] D.D. Fontaine, Cluster Approach to Order-Disorder Transformations in Alloys, in: Solid State Physics, Elsevier, 1994, pp. 33–176. https://doi.org/10.1016/S0081-1947(08)60639-6.

[38] D. Lerch, O. Wieckhorst, L. Hammer, K. Heinz, S. Müller, Adsorbate cluster expansion for an arbitrary number of inequivalent sites, Phys. Rev. B. 78 (2008), 121405, https://doi.org/10.1103/PhysRevB.78.121405.

[39] J.M. Sanchez, F. Ducastelle, D. Gratias, Generalized cluster description of multicomponent systems, Physica A 128 (1984) 334–350, https://doi.org/10.1016/0378-4371(84)90096-7.

[40] A. Seko, Y. Koyama, I. Tanaka, Cluster expansion method for multicomponent systems based on optimal selection of structures for density-functional theory calculations, Phys. Rev. B. 80 (2009), 165122, https://doi.org/10.1103/PhysRevB.80.165122.

[41] M.S. Daw, M.I. Baskes, Embedded-atom method: Derivation and application to impurities, surfaces, and other defects in metals, Phys. Rev. B. 29 (1984) 6443–6453, https://doi.org/10.1103/PhysRevB.29.6443.

[42] M.I. Baskes, Modified embedded-atom potentials for cubic materials and impurities, Phys. Rev. B. 46 (1992) 2727–2742, https://doi.org/10.1103/PhysRevB.46.2727.

[43] M.W. Finnis, J.E. Sinclair, A simple empirical N -body potential for transition metals, Philos. Mag. A 50 (1984) 45–55, https://doi.org/10.1080/01418618408244210.

[44] T. Kostiuchenko, F. Körmann, J. Neugebauer, A. Shapeev, Impact of lattice relaxations on phase transitions in a high-entropy alloy studied by machine-learning potentials, Npj Comput. Mater. 5 (2019) 55, https://doi.org/10.1038/s41524-019-0195-y.

[45] J.R. Winkler, Numerical recipes in C: The art of scientific computing, second edition, Endeavour. 17 (1993) 201. https://doi.org/10.1016/0160-9327(93)90069-F.

[46] G. Kresse, J. Furthmüller, Efficient iterative schemes for ab initio total-energy calculations using a plane-wave basis set, Phys. Rev. B. 54 (1996) 11169–11186, https://doi.org/10.1103/PhysRevB.54.11169.

[47] G. Kresse, J. Furthmüller, Efficiency of ab-initio total energy calculations for metals and semiconductors using a plane-wave basis set, Comput. Mater. Sci. 6 (1996) 15–50, https://doi.org/10.1016/0927-0256(96)00008-0.

[48] G. Kresse, J. Hafner, Ab initio molecular dynamics for liquid metals, Phys. Rev. B. 47 (1993) 558–561, https://doi.org/10.1103/PhysRevB.47.558.

[49] W. Kohn, L.J. Sham, Self-Consistent Equations Including Exchange and Correlation Effects, Phys. Rev. 140 (1965) A1133–A1138, https://doi.org/10.1103/PhysRev.140.A1133.

[50] P. Hohenberg, W. Kohn, Inhomogeneous Electron Gas, Phys. Rev. 136 (1964) B864–B871, https://doi.org/10.1103/PhysRev.136.B864.

[51] J.P. Perdew, K. Burke, M. Ernzerhof, Generalized Gradient Approximation Made Simple, Phys. Rev. Lett. 77 (1996) 3865–3868, https://doi.org/10.1103/PhysRevLett.77.3865.

[52] P.E. Blöchl, Projector augmented-wave method, Phys. Rev. B. 50 (1994) 17953–17979, https://doi.org/10.1103/PhysRevB.50.17953.

[53] G. Kresse, D. Joubert, From ultrasoft pseudopotentials to the projector augmented-wave method, Phys. Rev. B. 59 (1999) 1758–1775, https://doi.org/10.1103/PhysRevB.59.1758.

[54] V.T. Barone, B.R. Tuttle, S.V. Khare, Properties of AgBiI₄ using high through-put DFT and machine learning methods, J. Appl. Phys. 131 (2022), 245701, https://doi.org/10.1063/5.0088980.

[55] H. Zhu, A. Erbing, H. Wu, G.J. Man, S. Mukherjee, C. Kamal, M.B. Johansson, H. Rensmo, M. Odelius, E.M.J. Johansson, Tuning the Bandgap in Silver Bismuth Iodide Materials by Partly Substituting Bismuth with Antimony for Improved Solar Cell Performance, ACS Appl. Energy Mater. 3 (2020) 7372–7382, https://doi.org/10.1021/acsaem.0c00712.

[56] H.C. Sansom, G.F.S. Whitehead, M.S. Dyer, M. Zanella, T.D. Manning, M.J. Pitcher, T.J. Whittles, V.R. Dhanak, J. Alaria, J.B. Claridge, M.J. Rosseinsky, AgBiI₄ as a Lead-Free Solar Absorber with Potential Application in Photovoltaics, Chem. Mater. 29 (2017) 1538–1549, https://doi.org/10.1021/acs.chemmater.6b04135.

[57] J. Heyd, G.E. Scuseria, M. Ernzerhof, Hybrid functionals based on a screened Coulomb potential, J. Chem. Phys. 118 (2003) 8207–8215, https://doi.org/10.1063/1.1564060.

[58] G. Hautier, A. Miglio, D. Waroquiers, G.-M. Rignanese, X. Gonze, How Does Chemistry Influence Electron Effective Mass in Oxides? A High-Throughput Computational Analysis, Chem. Mater. 26 (2014) 5447–5458, https://doi.org/10.1021/cm404079a.

[59] M. Gajdoš, K. Hummer, G. Kresse, J. Furthmüller, F. Bechstedt, Linear optical properties in the projector-augmented wave methodology, Phys. Rev. B. 73 (2006), 045112, https://doi.org/10.1103/PhysRevB.73.045112.

[60] M. Nishiwaki, H. Fujiwara, Highly accurate prediction of material optical properties based on density functional theory, Comput. Mater. Sci 172 (2020), 109315, https://doi.org/10.1016/j.commatsci.2019.109315.

[61] T. Lam Pham, H. Kino, K. Terakura, T. Miyake, K. Tsuda, I. Takigawa, H. Chi Dam, Machine learning reveals orbital interaction in materials, Sci. Technol. Adv. Mater. 18 (2017) 756–765, https://doi.org/10.1080/14686996.2017.1378060.

[62] M. Rupp, A. Tkatchenko, K.-R. Müller, O.A. von Lilienfeld, Fast and Accurate Modeling of Molecular Atomization Energies with Machine Learning, Phys. Rev. Lett. 108 (2012), https://doi.org/10.1103/PhysRevLett.108.058301.

[63] F. Faber, A. Lindmaa, O.A. von Lilienfeld, R. Armiento, Crystal structure representations for machine learning models of formation energies, Int. J. Quantum Chem. 115 (2015) 1094–1101, https://doi.org/10.1002/qua.24917.

[64] N. Pai, J. Lu, T.R. Gengenbach, A. Seeber, A.S.R. Chesman, L. Jiang, D. C. Senevirathna, P.C. Andrews, U. Bach, Y. Cheng, A.N. Simonov, Silver Bismuth Sulfoiodide Solar Cells: Tuning Optoelectronic Properties by Sulfide Modification for Enhanced Photovoltaic Performance, Adv. Energy Mater. 9 (2019) 1803396, https://doi.org/10.1002/aenm.201803396.

[65] J. Even, L. Pedessseau, J.-M. Jancu, C. Katan, Importance of Spin-Orbit Coupling in Hybrid Organic/Inorganic Perovskites for Photovoltaic Applications, J. Phys. Chem. Lett. 4 (2013) 2999–3005, https://doi.org/10.1021/jz401532q.

[66] R. Das, S. Pandey, Comparison of Optical Properties of Bulk and Nano Crystalline Thin Films of CdS Using Different Precursors, Int. J. Mater. Sci. (2011).

[67] E. Nowak, M. Szybowicz, A. Stachowiak, W. Koczorowski, D. Schulz, K. Paprocki, K. Fabisiak, S. Los, A comprehensive study of structural and optical properties of ZnO bulk crystals and polycrystalline films grown by sol-gel method, Appl. Phys. A. 126 (2020) 552, https://doi.org/10.1007/s00339-020-03711-2.

[68] O.S. Center, Ohio supercomputer center, 1987.